Adaptive traveltime tomography of densely sampled seismic data

Immo Trinks,¹ Satish C. Singh,² Chris H. Chapman,³ Penny J. Barton,¹ Miguel Bosch⁴ and Adam Cherrett⁵

Accepted 2004 November 17. Received 2004 September 1; in original form 2004 April 8

SUMMARY

We present a new 2-D traveltime tomography method for the inversion of densely sampled seismic streamer data. This method was especially designed for the efficient inversion of longoffset multichannel data. A layer-interface model is used to fit ray-traced traveltime data to observed seismic data. The solution of the forward problem is based on initial-value ray tracing in a triangulated grid with a linear interpolation of the squared slowness. We implement an adaptive model parametrization based on ray density, which allows for smaller velocity cells with subsequent iteration steps. We solve the inverse problem using an iterative linearized joint inversion of reflection and refraction data for interface and velocity structures. Adaptive smoothing regularization is implemented in the form of a priori model covariances. As the cell sizes decrease with increasing iteration numbers, the model covariance ranges are reduced, allowing for more detail to emerge in the model. We demonstrate the algorithm's ability to invert successfully a realistic crustal velocity structure in a synthetic model. Several adaptive and non-adaptive model parametrizations are tested. The joint interface and velocity inversion of real long-offset reflection and refraction traveltime data is presented as a second example. We demonstrate that our results are in good agreement with independently derived velocity models.

Key words: controlled-source seismology, inversion, ray tracing, reflection seismology, refraction seismology, tomography, traveltime.

1 INTRODUCTION

Numerous techniques are in use to extract velocity information from seismic reflection data, such as semblance velocity analysis, refraction-slope measurements, and constant-velocity stacking (Yilmaz 1987; Sheriff & Geldart 1995). In recent years a more quantitative inversion approach has been used to extract velocity information from seismic data. Two types of seismic inversion are commonly used today: traveltime inversion (e.g. Phillips & Fehler 1991; Zelt & Barton 1998; Hobro et al. 2003) and full-waveform inversion techniques (e.g. Pratt et al. 1996; Zeev et al. 2001; Shipp & Singh 2002). In tomographic traveltime inversion, also referred to as traveltime tomography, seismic data are reduced to a number of traveltime picks corresponding to the arrival times of certain seismic phases. These traveltime values are inverted by automatically comparing them to synthetic data generated from a test model. This model may then be iteratively updated to reduce the data misfit by solving the non-linear inverse problem in linearized steps. The most commonly used forward modelling method to create this synthetic traveltime data is ray tracing.

A more holistic, but computationally more expensive, inversion technique is the waveform inversion method (Kormendi & Dietrich 1991). Its goal is to match real and synthetic wavefields, and consequently it has the potential to resolve much finer structures than inversion methods that are based on traveltimes alone (Pratt *et al.* 2002; Freudenreich 2002). Most full-waveform inversion schemes are based on steepest-descent or conjugate-gradient methods. Therefore, they require a starting model that is close to the real solution, so the inversion process is able to converge to the global minimum of the misfit function, as demonstrated by Failly *et al.* (1993). Traveltime inversion techniques may provide general constraints for the choice of such starting models. Furthermore, they are a good means of obtaining velocity models that can be used for pre-stack depth migration, especially in regions of complex geology, where standard velocity analysis fails (Yilmaz 1987).

The aim of traveltime tomography is to obtain a model for which the misfit between calculated and observed traveltime data is minimal (Scales & Smith 1997). Various approaches exist to search for the global minimum of the misfit function. One problem is that the solution might converge to a local minimum. Monte Carlo

© 2005 RAS

¹Bullard Laboratories, University of Cambridge, Madingley Road, Cambridge CB3 0EZ, UK. E-mail: trinks@esc.cam.ac.uk

²Laboratoire de Geosciences Marines, IPGP, Boite 89, 4 place Jussieu, 75252 Paris, France

³Schlumberger Cambridge Research, High Cross, Madingley Road, Cambridge CB3 OEL, UK

⁴Laboratorio N. 10 Simulacion e Inversión Geofísica, Facultad de Ingeniería, Universidad Central de Venezuela, Los Chaguaramos, Caracas, Venezuela

⁵Total Centre Scientifique et Technique Jean Feger, Avenue Larribau, 6400 Pau, France

methods are used if no analytical expressions for the relation between data and model parameters are available, or where the linearization of the problem fails (Mosegaard & Tarantola 1995). In the present case we use a linearized inversion, which assumes a linear relationship between small changes that are applied to the model and the corresponding change to the traveltime. Then the inversion proceeds in small steps towards the final solution. It is important to start as close as possible to the final solution in order to have a problem that is probably as linear as possible (Tarantola 1987).

Seismic inversion techniques involving densely sampled data are challenging due to the sheer amount of data. Multichannel streamer data sets acquired with two-ship survey geometries cover offset ranges of 18–30 km and contain valuable near- and far-offset reflection and refraction events. Since the seismic image quality increases with denser sampling, as many data as possible should be included in the analysis. Lutter *et al.* (1994) presented a high-resolution traveltime inversion of internal details of the Columbia River Basalt Group, including the basalt–sediment interface and the deeper sediment–basement interface. Even though this experiment involved more than 5000 observed traveltimes, the number of traveltime data obtained from marine seismic surveys exceeds this value by orders of magnitude. Therefore, in order to be able to invert marine seismic streamer data without discarding entire shot records, a new efficient traveltime inversion algorithm is needed.

Despite the range of existing traveltime tomography algorithms that are available to academic research it was considered necessary to develop a new traveltime tomography algorithm that is able to deal efficiently with the large amounts of data involved in high-resolution seismic surveys. The new algorithm should possess the following features compared with currently available algorithms:

- (i) flexible model parametrization based on triangulated velocity grids (Hale & Cohen 1991), in contrast to the restriction of defining velocities only along interfaces, as in the case of *RAYINVR* (Zelt & Smith 1992), for example;
- (ii) the option of adaptive parametrization, which can easily be implemented in triangulated grids (Böhm *et al.* 2000), in contrast to regular blocky models;
- (iii) efficient ray tracing based on the shooting method, in contrast to solving the two-point problem, as performed by, for example, *Jive3D* (Hobro 1999);
- (iv) the ability to invert other than first arrivals, in contrast to *FAST* (Zelt & Barton 1998), for instance.

In this paper we describe first the formulation of the new traveltime tomography algorithm in respect to model parametrization and the solution of the forward and inverse problems. Secondly, a synthetic inversion test is presented, demonstrating the successful recovery of the long-wavelength structure of the initial model. Finally, we present the application of the algorithm to a real seismic data set from the North East Atlantic.

2 TOMOGRAPHY APPROACH

Our approach to model parametrization, ray tracing and inversion is based on the method of McCaughey & Singh (1997) and Hobro *et al.* (2003), but allows for irregular parametrized velocity grids based on Delaunay triangulation. Since the geometry of very long-offset marine seismic reflection surveys can be regarded as 2-D, the algorithm was developed for 2-D applications.

2.1 Model parametrization

The appropriateness of model parametrization and display of results is crucial to the tomographic problem (Kissling *et al.* 2001). The

choice of parametrization constrains the possible solutions for both the forward and inverse problems. In general, models used in traveltime tomography are either over- (Hobro *et al.* 2003) or under- (Zelt & Smith 1992) parametrized relative to the number of data used. Here we are proposing to use an optimal model parametrization.

The algorithm presented here is based on Delaunay triangulated grids with velocities defined at the triangle vertices. Within each triangle the slowness squared is interpolated linearly. Models using the slowness square to define velocity distributions have been referred to as *sloth models* (Muir & Dellinger 1985). Such sloth models allow for a fast analytic solution of the ray-tracing equations while avoiding discontinuities in the ray path that would occur when using cells of constant velocity (Červený 2001). Regularly and irregularly distributed velocity nodes are gridded using the efficiently formulated sweepline algorithm (Fortune 1987) for triangulation.

In triangulated grids the ability to determine whether a triangle contains a given point is needed. Shirley (1992) described such a method based on barycentric coordinates. Given the coordinates of a point *P*, the corresponding triangle can be found by testing all triangles in the grid. We use the far more efficient *walking triangle algorithm* (Sambridge *et al.* 1995) to locate the triangle that contains *P*. The efficiency can be further increased by subdividing the model space using spatial division tables.

Having identified the triangle that contains a certain point we need to be able to ascertain the physical properties, such as seismic velocity, slowness, or squared slowness, at that point. Since these properties are defined only at the node points of the triangulated grid we need to interpolate them within the grid. A linear interpolation was chosen because a linear gradient of the slowness squared allows for an analytic solution of the forward problem (Appendix A). In addition, linear interpolation does not alter the velocities at the grid points, therefore allowing a better control over the velocity field. In contrast, a B-spline interpolation could lead to an interpolated velocity field that does not coincide with the node values and non-analytic solutions of the forward problem.

It is desirable that the parameter density should be modifiable depending on the regions of the model that are illuminated by rays. Such an adaptive parametrization would not only avoid instability in the inversion but also increase the efficiency of the algorithm. Vesnaver (1994) and Böhm & Vesnaver (1996) describe an inversion algorithm that reduces the non-uniqueness of the traveltime inversion result by adapting the grid. The shape of grid cells and the number of grid nodes are modified while the null-space energy is used as a data-independent measure for the inversion reliability. Faletič (1997) presents a self-adaptive global seismic tomography method based on gradient-driven mesh refinement through cell bisection, and highlights the problem of optimizing both the number of parameters employed and the model fit, suggesting a combination of regular and irregular refinements of the model. The data-driven approach proposed by Cox & Verschuur (2001) seems to overcome this problem by applying a stable and well-determined updating procedure that makes use of the a posteriori covariance. In their approach the local adjustment of the Delaunay triangulated grid depends on the variance of the model parameters after model optimization in the inversion step. Starting with a small number of parameters the model will behave in such a way that it will grow towards its final solution (Cox & Verschuur 2001). Here, an adaptive gridding procedure that increases the number of velocity node points in the model, based on the ray density, was implemented.

One method to increase the node density of an initially regular grid of equilateral triangles would be through triangle subdivision, by placing an additional grid point in the triangle's centroid.

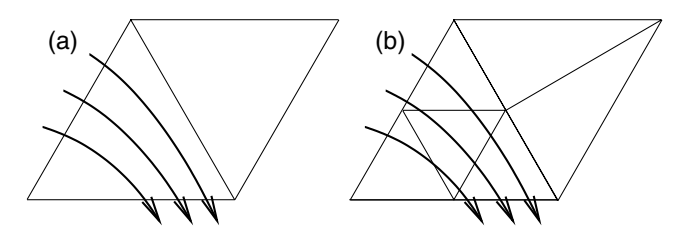


Figure 1. Subdivision of equilateral triangles. (a) Triangles with and without intersecting rays. (b) Subdivision of the triangle with ray coverage into four likewise equilateral triangles. The length of the new triangle sides is half that of the original triangle. The neighbouring triangle without intersecting rays is subdivided into two right-angled triangles.

However, the resulting triangles would not be equilateral, and after few recursive subdivisions the grid would consist of many narrow triangles. Such a subdivision is undesirable since the intrinsic numerical errors of the ray tracing become more important if a ray has to pass through a large number of narrow triangles. Therefore, the following method for subdivision of a regular triangulated grid, in which most of the subtriangles remain equilateral, has been implemented. New grid points are inserted at the median of each triangle side, for all triangles that are intersected by one or more rays (Fig. 1a). Triangles without any crossing rays, but located next to triangles with intersecting rays, are subdivided into two right-angled triangles. All other triangles in the grid remain unchanged. At secondary subdivision steps, it is possible that the bordering triangles could become less regular, since rays at the edge of the ray fan might intersect non-equilateral triangles.

Interfaces between velocity grids representing the various layers are implemented in the model parametrization of the present inversion algorithm. Each interface is defined by at least two interface nodes, with horizontal position, depth and depth gradient assigned. Currently only one depth gradient is attached to each interface node, but the algorithm may be extended in the future to include separate gradients on either side of the node, allowing sharp kinks in the interface. Between interface nodes the shape of the interface is interpolated using a cubic Hermite interpolation that is based on the coordinate information of the two interface nodes and the two corresponding interface depth gradients (Appendix B). A simple horizontal interface may be defined by two interface nodes.

After the creation of an interface, the interface node density is increased automatically by interpolation at regular intervals. This operation guarantees the minimum density of interface nodes that is required by the interface inversion algorithm. This value can be tuned as required in order to avoid over- or under-parametrized interfaces and to account for the local resolution and ray coverage. Interface nodes on different interfaces can possess the same coordinate values, so that it is possible to define layers that pinch out, or layers of zero thickness. Furthermore, it is possible to assign additional attributes to the interface nodes which would flag parts of an interface active, while other segments of the interface are inactive; on the basis of such labelling, it would be possible to construct interfaces that extend only over parts of the model, so that reflections are generated only when a ray hits an active segment of an interface.

Since the position of interfaces will be allowed to change during the inversion process it is important that the grids extend over a range that is large enough to accommodate these changes. Within the model each layer is defined by its Delaunay triangulated grid and an upper and lower interface. After the allocation of the corresponding grids and interfaces, every triangle that is intersected by an interface is marked with a flag. This procedure permits efficient ray tracing, since each ray will only look out for a ray—interface intersection in the case where it enters a marked triangle. Otherwise it will proceed rapidly to the next triangle along its path. This flagging procedure is repeated every time the interfaces are changed during the inversion process.

2.2 Solving the forward problem

The forward problem of the inversion is solved using efficient analytical ray tracing in a medium with a linear gradient of slowness squared, as formulated by Farra (1990) and Červený (2001). Instead of solving the two-point problem, an initial-value ray-tracing scheme with traveltime interpolation is implemented. It is possible to increase the ray density at low cost such that at least one ray emerges between each receiver pair, wherever this is physically possible.

In 2-D media the square of the slowness u at the position \mathbf{x} may be defined as

$$u^{2}(\mathbf{x}) = u_{0}^{2} + \mathbf{\Gamma} \cdot (\mathbf{x} - \mathbf{x}_{0}), \tag{1}$$

with

$$\Gamma = \nabla u^2 \tag{2}$$

as the gradient of the squared slowness and u_0 as the slowness at location \mathbf{x}_0

The ray path within a triangle and its corresponding traveltime can be described analytically using the expressions for Γ and u_0 . The ray-tracing equations can be expressed according to Farra (1990) as

$$\mathbf{p}(\tau) = \frac{1}{2} \mathbf{\Gamma}(\tau - \tau_0) + \mathbf{p}(\tau_0), \tag{3}$$

and

$$\mathbf{x}(\tau) = \frac{1}{4} \mathbf{\Gamma}(\tau - \tau_0)^2 + (\tau - \tau_0) \mathbf{p}(\tau_0) + \mathbf{x}(\tau_0), \tag{4}$$

where **p** describes the slowness of the ray, the ray parameter, τ is a sampling variable that increases monotonically along the ray, τ_0 is defined as the initial value of τ when the ray enters a triangle, and **x** is the ray position. The total traveltime T can be computed as

$$T(\tau) = T(\tau_0) + \left[u_0^2 + \mathbf{\Gamma} \cdot \mathbf{x}(\tau_0)\right](\tau - \tau_0)$$
$$+ \frac{1}{2}\mathbf{\Gamma} \cdot \mathbf{p}(\tau_0)(\tau - \tau_0)^2 + \frac{1}{12}\mathbf{\Gamma}^2(\tau - \tau_0)^3. \tag{5}$$

Given the position and direction of the ray as it enters a triangle, the algorithm computes the ray exit position, the ray direction in this position, and the traveltime through this triangle. Furthermore, the ability to determine the exact location of the ray inside the triangle at an arbitrary point along the ray trajectory is given by eq. (4). This feature is needed for the location of intersections of the ray with possible interfaces or receiver arrays.

When the ray enters a triangle that contains an interface or streamer segment, the analytical ray-tracing procedure is interrupted and the ray—interface or ray—streamer intersection calculated numerically. Beginning from the point at which the ray enters a triangle, the method progresses along the ray in small steps and evaluates whether the test point is still on the same side of the interface as the starting point. For the case of a ray—streamer intersection, the algorithm tests the ray position against the constant streamer depth. The stepping procedure is stopped if the interface or receiver array is crossed. Two distinct algorithms are implemented to find the ray—interface or ray—streamer intersections within the remaining interval: Newton—Raphson and bi-section. Bi-section means that the remaining interval of the ray path within the triangle is divided into

two equally long sections and a test is applied to determine whether the half-way point is still on the same side of the interface. This procedure is applied successively until the solution is found within the limits of the predefined tolerance range. The convergence of the bisection method is linear within the required accuracy and therefore it is not the most efficient way to calculate the intersection (Press *et al.* 1992).

As a more efficient procedure the Newton–Raphson algorithm is employed, which has a quadratic convergence at best (Press *et al.* 1992). The method works by extrapolating the local derivative, which is the tangent to the ray, to find the next estimate of the ray–interface intersection. Subsequent test points along the ray are found at the crossing between the ray and the normal to the interface in the estimated solution. This procedure is repeated until the ray–interface intersection is located within the given tolerance, which may be tuned according to the problem. In the case of local extremes in the ray path, it is possible that the solution diverges. For such situations, a counter is implemented into the Newton–Raphson algorithm that causes the iteration loop to break after a predefined number of iterations, and to fall back to the slower but safer bisection algorithm.

Snell's law for reflection and refraction at an interface is implemented as a vector formulation, avoiding trigonometric functions. For the reflection case, the direction of the reflected ray ${\bf R}$ is given by

$$\mathbf{R} = \mathbf{I} - 2(\mathbf{I} \cdot \mathbf{N})\mathbf{N},\tag{6}$$

with I as the slowness vector of the incident ray and N as the normal to the interface. In the transmission case, the direction T of the refracted ray is obtained by solving the expression

$$\mathbf{T} = \mathbf{I} + x\mathbf{N} \tag{7}$$

for x. By splitting eq. (7) into components that are perpendicular and parallel to the interface and making use of the fact that $|T| = u^2$, with u^2 being the squared slowness of the second medium at the intersection position, eq. (7) can be transformed into the quadratic polynomial

$$x^{2} + 2x(\mathbf{I} \cdot \mathbf{N}) + |\mathbf{I}|^{2} - u^{2} = 0.$$
(8)

There are potentially two solutions to eq. (8), but only one relates to a ray propagating in the second medium. The correct solution may be selected by comparing the signs of the components normal to the interface:

$$(\mathbf{I}.\mathbf{N})(\mathbf{T}.\mathbf{N}) > 0. \tag{9}$$

If no real roots exist for eq. (8), total internal reflection occurs and no transmitted events are possible.

Each individual ray is constructed of single segments that describe the path and traveltime of the ray within each of the triangles the ray passes through. These ray segments are grouped together to form macro ray segments for every layer. All macro ray segments together form the entire ray from its source to its end position. The traveltime of the ray is calculated by summation of the individual ray-segment contributions. Within each ray segment the traveltime is computed analytically and the position ${\bf x}$ at which the ray leaves a triangle and its local direction ${\bf p}$ are passed on as entry parameters to the consecutive triangle.

2.3 Formulating the inversion

In order to be able to minimize the misfit between modelled and observed traveltimes, a measure is needed to link the change in

traveltime to a change in model parameter. This relation has to be established for every model parameter. The linearizing assumption of the inversion requires this change in model parameter to be small. To obtain this relation, one possible approach is to solve the twopoint problem for a large number of rays, and applying small model perturbations for each model parameter in turn. Thus, the effect of a change in the model can be linked to a change in traveltime of affected rays. However, this method is extremely inefficient. The model parametrization and the ray-tracing approach chosen in this work allow for an efficient analytical computation of the so-called Fréchet derivatives of traveltime with respect to model parameters. In Appendix C we show how the Fréchet derivatives are obtained for the velocity and interface parameters. The Fréchet derivative computation is limited to those model parameters that affect the traveltime of a ray. These parameters are all the velocity nodes that belong to triangles that are intersected by the rays, and the interface nodes that have a ray intersecting or reflecting from a part of the interface next to them. Changes applied to any other model parameter would not affect the traveltime of this ray, and therefore the corresponding Fréchet derivatives are set to zero. The procedure followed is to step along every ray and to compute the Fréchet derivatives for all the model parameters that are encountered.

2.3.1 The optimization function

The solution of the inverse problem involves a search over the model space for the most plausible model **m** that is able to explain the recorded data **d**. In the case of traveltime tomography these data are picked traveltimes. A starting model is chosen for the inversion that is likely to be close to the real subsurface velocity distribution. Rays are traced in this model in order to obtain a first set of synthetic traveltimes. The comparison of these computed traveltimes with the actually measured data results in the data misfit, or data residual

$$\Delta \mathbf{d} = \mathbf{d}_{\text{obs}} - \mathbf{d}_{\text{m}},\tag{10}$$

with \mathbf{d}_{obs} as the observed, and \mathbf{d}_m as the modelled data. The number of parameters used in the computation is much too large to search the complete model space for the model that minimizes this residual best. Under the assumption that small changes of the model $\Delta \mathbf{m}$ result in only small changes in the data $\Delta \mathbf{d}$, so that the new model remains in the region of linearity that surrounds the previous model, a linear relationship may be established (Indira & Gupta 1998):

$$\Delta \mathbf{d} \approx \mathbf{G} \Delta \mathbf{m},$$
 (11)

where G is the matrix that contains the partial derivatives of the data with respect to the model parameters, the Fréchet derivatives. The size of G is the number of data times the number of model parameters. Since any particular ray intersects just a few triangles in our model, only a small number of model parameters affect this ray. Therefore, most elements of the matrix G will be zero. Such a sparse matrix can be stored efficiently as described by Press *et al.* (1992).

Here, the following approach is taken to calculate the model update $\Delta \mathbf{m}$. In order to reduce the misfit \mathbf{r} between the observed data \mathbf{d}_{obs} and the modelled data \mathbf{d}_{m} an objective function S is formulated:

$$S = (\underbrace{\mathbf{d}_{\text{obs}} - \mathbf{d}_{\text{m}}}_{\mathbf{r}})^{\text{T}} \mathbf{C}_{\text{d}}^{-1} (\underbrace{\mathbf{d}_{\text{obs}} - \mathbf{d}_{\text{m}}}_{\mathbf{r}}) + \Psi, \tag{12}$$

where \mathbf{C}_d^{-1} is the inverse data covariance matrix containing the data uncertainties σ_d . The matrix \mathbf{C}_d^{-1} , like \mathbf{C}_d , is diagonal due to the assumption that the covariance between any non-identical pair of

data is zero (Hobro 1999). The term Ψ in eq. (12) is a regularization term with the task of constraining the inversion, as described in the following section.

2.3.2 Regularization of the inversion

In addition to the data misfit term of the objective function S we require a further term Ψ that regularizes the inversion process. This regularization term allows us to influence the inversion such that models with specific attributes are favoured, while models with undesirable properties are penalized. The regularization approach described here is based on the definition of a model covariance matrix \mathbf{C}_{m} (e.g. Tarantola & Valette 1982; Korenaga *et al.* 1997; Soupios *et al.* 1999). This matrix contains information on the variability allowed for each model parameter, as well as their spatial correlations. The model covariance matrix \mathbf{C}_{m} may be used to describe how a change in one model parameter affects its neighbouring parameters. The inverse model covariance matrix is divided into two parts, one representing the velocity parameters [$\mathbf{C}_{\mathrm{v}}^{-1}$], and the other representing the interface parameters [$\mathbf{C}_{\mathrm{i}}^{-1}$]:

$$\mathbf{C}_{\mathrm{m}}^{-1} = \begin{bmatrix} \mathbf{C}_{\mathrm{v}}^{-1} & \mathbf{0} \\ \mathbf{0} & \mathbf{C}_{\mathrm{i}}^{-1} \end{bmatrix}. \tag{13}$$

The zeros in eq. (13) indicate that the cross-correlation between the velocity and interface parameters is assumed to be zero.

Model covariances are defined in the following way. The distance *d* between two velocity nodes is calculated as

$$d^2 = \left(\frac{h_x}{\Delta a_x}\right)^2 + \left(\frac{h_z}{\Delta a_z}\right)^2,\tag{14}$$

with h_x and h_z as the horizontal and vertical components of the vector between the node points, and Δa_x and Δa_z as the covariance influence ranges in the horizontal and vertical directions respectively. These covariance influence ranges are defined *a priori*, and may be obtained from geostatistical analysis, for example via interpretation of stacked seismic sections (Bosch *et al.* 2002a) or from well log data.

Three commonly used covariance functions (Isaaks & Srivastava 1989) are implemented into the model covariance matrix calculation.

(i) Gaussian:

$$cov = n\sigma^2 e^{-3d^2},\tag{15}$$

(ii) Spherical:

$$cov = n\sigma^2(1 - 1.5d + 0.5d^3)$$
 if $h < a$, (16)

$$= 0 \quad \text{if} \quad h > a, \tag{17}$$

(iii) Exponential:

$$cov = n\sigma^2 e^{-3d}, (18)$$

with σ as the variance parameter and cov as the velocity covariance. The factor n, which is referred to as the nugget, is a value that represents the inherent variability of the data. A small value of n should always be used in order to avoid numerical problems with ill-conditioned matrices. The Gaussian covariance function is well adapted to smooth fields, since in this case the covariance stays high in the vicinity of a node point. An exponential function is more suited to rough fields in which the covariance decreases rapidly (Dubrule 2003). The tomographic inversions described below use a Gaussian covariance distribution.

Now, the regularization term Ψ can be written as

$$\Psi = (\mathbf{m}_{n+1} - \mathbf{m}_{\text{prior}})^{\mathrm{T}} \mathbf{C}_{m}^{-1} (\mathbf{m}_{n+1} - \mathbf{m}_{\text{prior}}). \tag{19}$$

Under the linearizing assumption of eq. (11), the data of the (n + 1)th iteration can be expressed as

$$\mathbf{d}(\mathbf{m}_{n+1}) = \mathbf{d}(\mathbf{m}_n) + \mathbf{G}(\underbrace{\mathbf{m}_{n+1} - \mathbf{m}_n}_{\text{Am}_n}), \tag{20}$$

with $\Delta \mathbf{m}_n$ as the *n*th model update. The objective function *S* can then be written as

$$S(\mathbf{m}_{n+1}) = (\mathbf{r} - \mathbf{G}\Delta\mathbf{m}_n)^{\mathrm{T}} \mathbf{C}_{\mathrm{d}}^{-1} (\mathbf{r} - \mathbf{G}\Delta\mathbf{m}_n)$$

$$+ (\mathbf{m}_{n+1} - \mathbf{m}_{\mathrm{prior}})^{\mathrm{T}} \mathbf{C}_{\mathrm{m}}^{-1} (\mathbf{m}_{n+1} - \mathbf{m}_{\mathrm{prior}}).$$
(21)

Hence, the gradient of *S* is calculated as

$$\nabla S = -2\mathbf{G}^{\mathrm{T}}\mathbf{C}_{\mathrm{d}}^{-1}(\mathbf{r} - \mathbf{G}\Delta\mathbf{m}_{n}) + 2\mathbf{C}_{\mathrm{m}}^{-1}(\underbrace{\mathbf{m}_{n} + \Delta\mathbf{m}_{n}}_{\mathbf{m}_{n+1}} - \mathbf{m}_{\mathrm{prior}}). \quad (22)$$

In order to find the model update $\Delta \mathbf{m}_n$ that minimizes the residual \mathbf{r} , ∇S is set to zero, resulting in

$$\mathbf{G}^{\mathrm{T}}\mathbf{C}_{\mathrm{d}}^{-1}\mathbf{r} - \mathbf{C}_{\mathrm{m}}^{-1}(\mathbf{m}_{n} - \mathbf{m}_{\mathrm{prior}}) = (\mathbf{G}^{\mathrm{T}}\mathbf{C}_{\mathrm{d}}^{-1}\mathbf{G} + \mathbf{C}_{\mathrm{m}}^{-1})\Delta\mathbf{m}_{n}.$$
 (23)

This equation can be transformed into a formulation that does not contain $C_{\rm m}^{-1}$, which to obtain is computationally expensive:

$$\underbrace{\mathbf{C}_{\mathbf{m}}\mathbf{G}^{\mathsf{T}}\mathbf{C}_{\mathbf{d}}^{-1}(\mathbf{d}_{\mathrm{obs}}-\mathbf{d}_{m_{n}})+(\mathbf{m}_{\mathrm{prior}}-\mathbf{m}_{n})}_{= \underbrace{\left(\mathbf{C}_{\mathbf{m}}\mathbf{G}^{\mathsf{T}}\mathbf{C}_{\mathbf{d}}^{-1}\mathbf{G}+\mathbf{I}\right)}_{\mathbf{\Delta}\mathbf{m}_{n}}, \tag{24}$$

with the identity matrix **I**. In the case of the first iteration ($\mathbf{m}_{prior} - \mathbf{m}_1$) = 0. Eq. (24) can be regarded as the simple linear equation

$$\mathbf{b} = \mathbf{A}\mathbf{x},\tag{25}$$

where $\bf A$ is the curvature of the misfit function S, and $\bf b$ is the direction of its steepest gradient. Eq. (25) can be solved using the biconjugate gradient algorithm, which is a generalized form of the conjugate gradient algorithm, allowing the minimization of linear equations that are not necessarily symmetric (Press *et al.* 1992). This algorithm is fast and accurate and takes advantage of the sparsity of the matrices $\bf G$ and $\bf C_m$.

The joint inversion of interface depth and velocity involves two independent types of parameters with different units (km and km $\rm s^{-1}$) of unequal magnitude. The relative variability in the solution of the two types of parameters is related to the choice of variances in the prior model covariance matrix.

3 SYNTHETIC INVERSION TEST

The new traveltime tomography algorithm was tested for an unknown realistic crustal 2-D velocity model. This blind test was set up by Colin Zelt and John Hole for the CCSS Workshop¹ held in October 2003. The model that was used to generate the data for this test is 250-km long and extends to a depth of 40 km (Fig. 4d). Synthetic wide-angle data were calculated with a 2-D viscoelastic code for 51 shots with 5-km spacing. Traveltime data were provided for 2779 receivers with 90-m spacing for each shot, with a constant picking uncertainty of 25 ms (Fig. 2).

First-arrival traveltime tomography was performed using turning rays in a single-layer model. The starting model was defined using

¹http://www.geophysics.rice.edu/department/faculty/zelt/ccss/

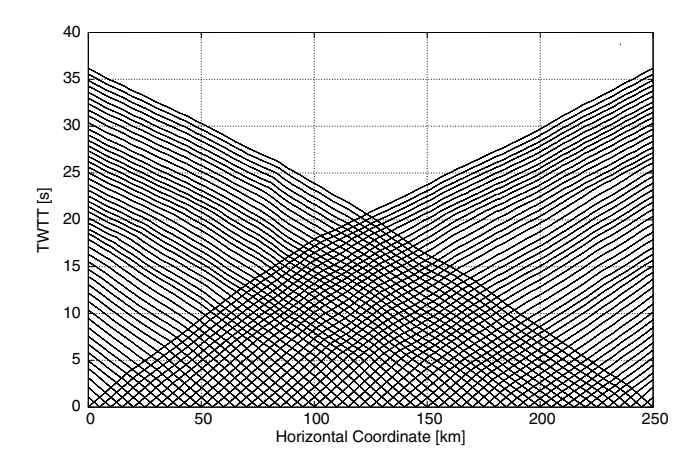


Figure 2. 141 729 first-arrival traveltime data provided by Colin Zelt as input to the inversion. The picking uncertainty was set to a constant value of 25 ms

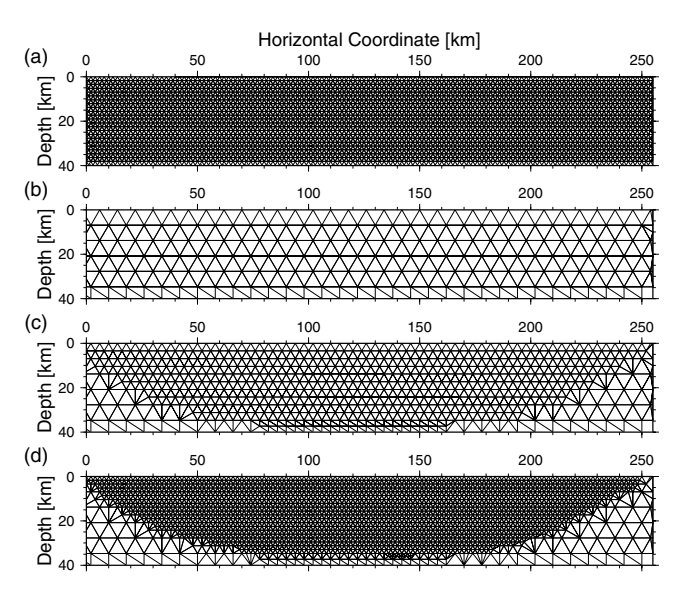


Figure 3. (a) Non-adaptive, and (b)–(d) adaptive gridding for the inversion of the unknown velocity model. (a) Non-adaptive grid used in the inversion of case three (regular triangle side length 2 km). (b) Parametrization for the starting model of case four (regular triangle side length 8 km). (c) Grid densification after three inversion steps (regular triangle side length 4 km). (d) Final grid densification after 10 inversion steps (regular triangle side length 2 km).

a linear vertical velocity gradient between 4.0 km s^{-1} at the surface and 8.0 km s^{-1} at 40-km depth. Four different velocity grid parametrizations were tested.

- (i) In the first case, the side length of the equilateral triangles in the velocity grid was set to a constant value of to 5 km throughout the inversion, using horizontal and vertical covariance ranges of 20 km and 10 km, respectively.
- (ii) In the second case, the velocity grid consisted of equilateral triangles with 3-km side length, using horizontal and vertical covariance ranges of 3 km.
- (iii) In the third case, the grid consisted of equilateral triangles with 2-km side length (Fig. 3a), using horizontal and vertical covariance ranges both of 4 km.
- (iv) In the fourth case, adaptive grid parametrization and covariance ranges were chosen. The first three iterations were performed

in a velocity grid consisting of equilateral triangles of 8-km side length (Fig. 3b). Then, all triangles that were intersected by at least three rays were subdivided into four regular triangles of 4-km side length (Fig. 3c). A second grid refinement was performed after 10 inversion iterations in total, resulting in triangles of 2-km side length in the region covered by rays (Fig. 3d). The corresponding horizontal and vertical covariance ranges were adapted from 20 km and 10 km for the first three iterations, to 10 km and 5 km for iterations 3 to 10, and to 3 km and 3 km for iterations 10 to 20.

The χ^2 for all four cases are shown in Fig. 5. All curves converged after 20 iterations: for case one to 3.1, for case two to 1.86 and for cases three and four both to 1.04. The larger remaining χ^2 values for cases one and two illustrate that model variations on a scale smaller than 3 km are required to fit the data satisfactorily. The χ^2 curves for cases one, two and three show that smaller cell sizes lead to slower convergence rates. The adaptive parametrization in case four combines the fast convergence for large cells with a small final χ^2 value of 1.04. The grid refinement after three and 10 inversion iterations can be seen in the χ^2 curve of case four as a slight increase.

The inversion results for cases three and four are shown in Figs 4(a) and (b). The resulting velocity models differ in character. In case three the region covered by rays is smaller than in case four, and velocity anomalies are smeared along the ray paths (Fig. 4a). The model obtained using the adaptive parametrization and regularization appears smoother and more detailed (Fig. 4b). Case four leads to a model with minimum structure that allows the data to be fitted within the picking uncertainty to an almost ideal value (1.04) and is therefore the preferred model for this inversion test. Adaptive parametrization progressing from large grid cells to smaller triangles leads to a recovery of the long-wavelength structures first, and the subsequent addition of more detail at later iterations. This effect is supported by the adaptive regularization with decreasing covariance ranges for later inversion stages. The initial recovery of the largescale features of the model in the case of adaptive parametrization and regularization permits greater illumination at later stages of the inversion.

The quality of the model recovery can be seen in the vertical and horizontal velocity profiles shown in Figs 6 and 7. Velocities for the starting model used in the inversion, for the inversion result, for the CCSS model, and for a filtered version of the CCSS model (Gaussian filter with 10-km width and 5-km height) are plotted. The vertical velocity profiles taken at 100 km and 200 km horizontal coordinate demonstrate a good recovery of the velocity model. The horizontal velocity profiles in Fig. 7 demonstrate the effect of decreasing ray coverage at the sides of the model with increasing depth. Traveltime tomography is not suited to the recovery of the small-scale velocity variations that can be seen in the CCSS test model velocity profiles. However, the smooth velocity model provided by traveltime inversion may be used as the starting model for computationally more expensive techniques, such as full-waveform inversion. The vertical velocity profile taken at 200-km distance shows that the low-velocity anomaly at about 8-km depth is indicated in the inversion result.

4 INVERSION OF A REAL LONG-OFFSET SEISMIC DATA SET

The new traveltime inversion algorithm was next applied to a largeaperture reflection seismic data set, acquired at the North East Atlantic Margin in 1997. The objective of this experiment was the production of a seismic image and velocity profile of the geology beneath basaltic layers using both near- and far-offset data. One

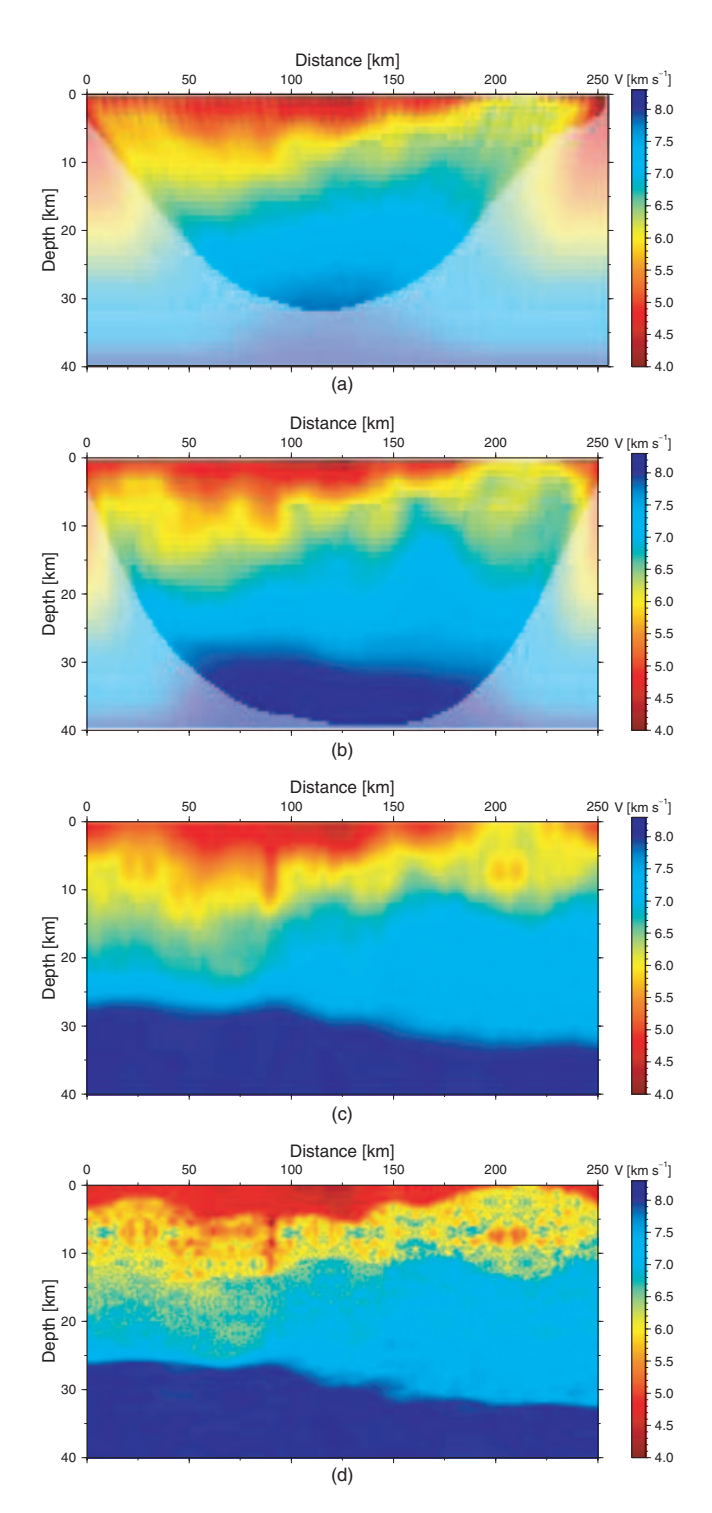


Figure 4. (a) Inversion result after 20 iterations for the non-adaptive inversion (case three). (b) Inversion result after 20 iterations for the adaptive inversion (case four). The ray coverage in (a) and (b) is indicated by shading the unconstrained regions of the models. (c) The true velocity model filtered with a Gaussian filter (width 10 km, height 5 km) for comparison with the results obtained in this study. (d) The true velocity model that was used for the generation of the traveltime data shown in Fig. 2.

single seismic line was recorded as a synthetic aperture profile with two passes of two vessels, and a constant vessel offset of 12 km and 24 km respectively for each pass. Both ships towed 6-km-long streamers and each had a 5800-cubic-inch source array. The sources

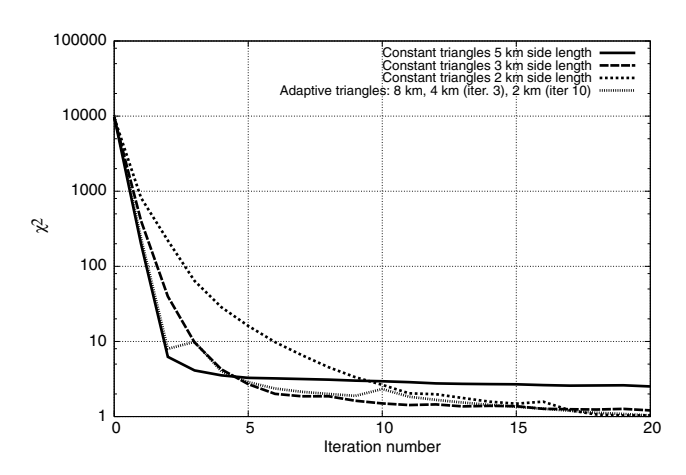


Figure 5. χ^2 values after 20 iterations for the models parametrized using constant triangles of 5 km side length (case 1), constant triangles of 3 km side length (case 2), constant triangles of 2 km side length (case 3), and the adaptive parametrization using triangle side lengths of 8, 4 and 2 km side lengths (case 4). This figure shows that fine parametrization is needed to reach χ^2 values close to 1.

were fired alternately with an overall shot interval of 50 m, and a shot interval of 100 m for each vessel. The hydrophone group spacing within each streamer was 25 m, the sampling interval 4 ms, and the maximum recording length 18 s. This recording geometry resulted in data over an offset range from 175 m to 30 km. In total, about 700 shot super-gathers with offsets up to 30 km were provided. An example shot super-gather with traveltime picks superimposed is shown in Fig. 8. These data and traveltime picks are the subject of the processing, traveltime inversion, and discussion presented below.

The survey described here was especially designed to image structures below extrusive basalt flows and intrusive sills that were emplaced along the North Atlantic Margin through Tertiary volcanic episodes (Joppen & White 1990; England & Hobbs 1997). Hydrocarbon reservoirs are thought potentially to be trapped in Mesozoic sediments underneath the basaltic cover (Roberts et al. 1999). With the extension of oil and gas exploration into deep-water frontier regions, sub-basalt imaging techniques are becoming increasingly interesting. Furthermore, knowledge about the structure of the basement in this region is of importance for the understanding of basin evolution. Standard seismic reflection profiling fails to record subbasalt events, since the strong impedance contrast at the sedimentbasalt interface allows only little energy to penetrate into deeper layers. In addition, complex multiples are generated at the top basalt interface, whose rough surface results in scattering of the energy and in poor signal-to-noise ratios. These difficulties might be overcome when seismic energy is recorded at very large offsets. Refracted energy and long-offset reflections as well as converted phases could be used to study the thickness and geometry of the basalt layers, the sediments, and the basement below. The traveltime tomographic technique described above should be able to recover a smooth velocity model from the data.

Bosch *et al.* (2002a) have independently inverted this data set using a geostatistical traveltime inversion method, based on the modelling and ray-tracing algorithm described by Hobro *et al.* (2003). The major difference from this work is that our parametrization is based on an adaptive triangulated grid, whereas in the referenced work the parametrization is fixed. In order to be able to compare the result obtained with the new algorithm to the findings of Bosch

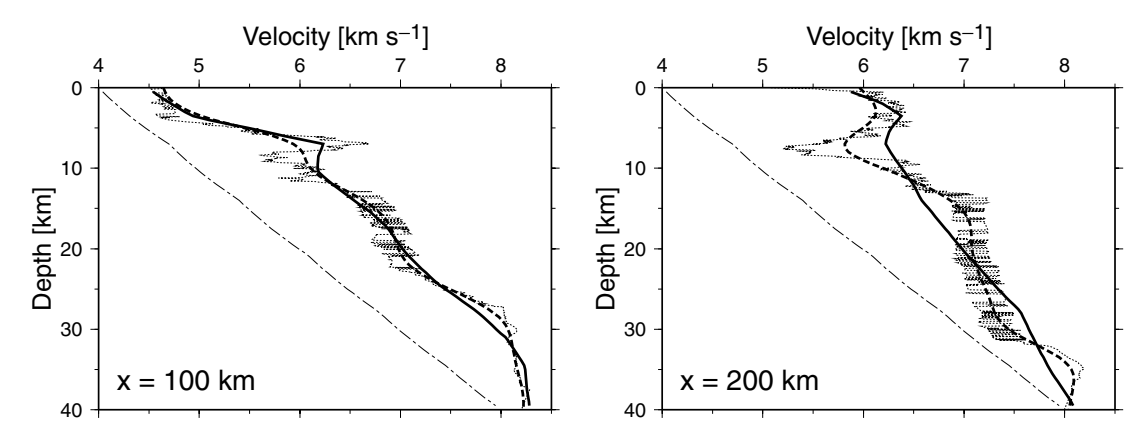


Figure 6. Vertical velocity profiles through the CCSS velocity model (thin dotted line), the filtered CCSS model (thick dashed line), and the adaptive inversion result (thick solid line) for constant horizontal coordinates of 100 km and 200 km. The velocity in the starting model is shown as a thin line with alternating dots and dashes.

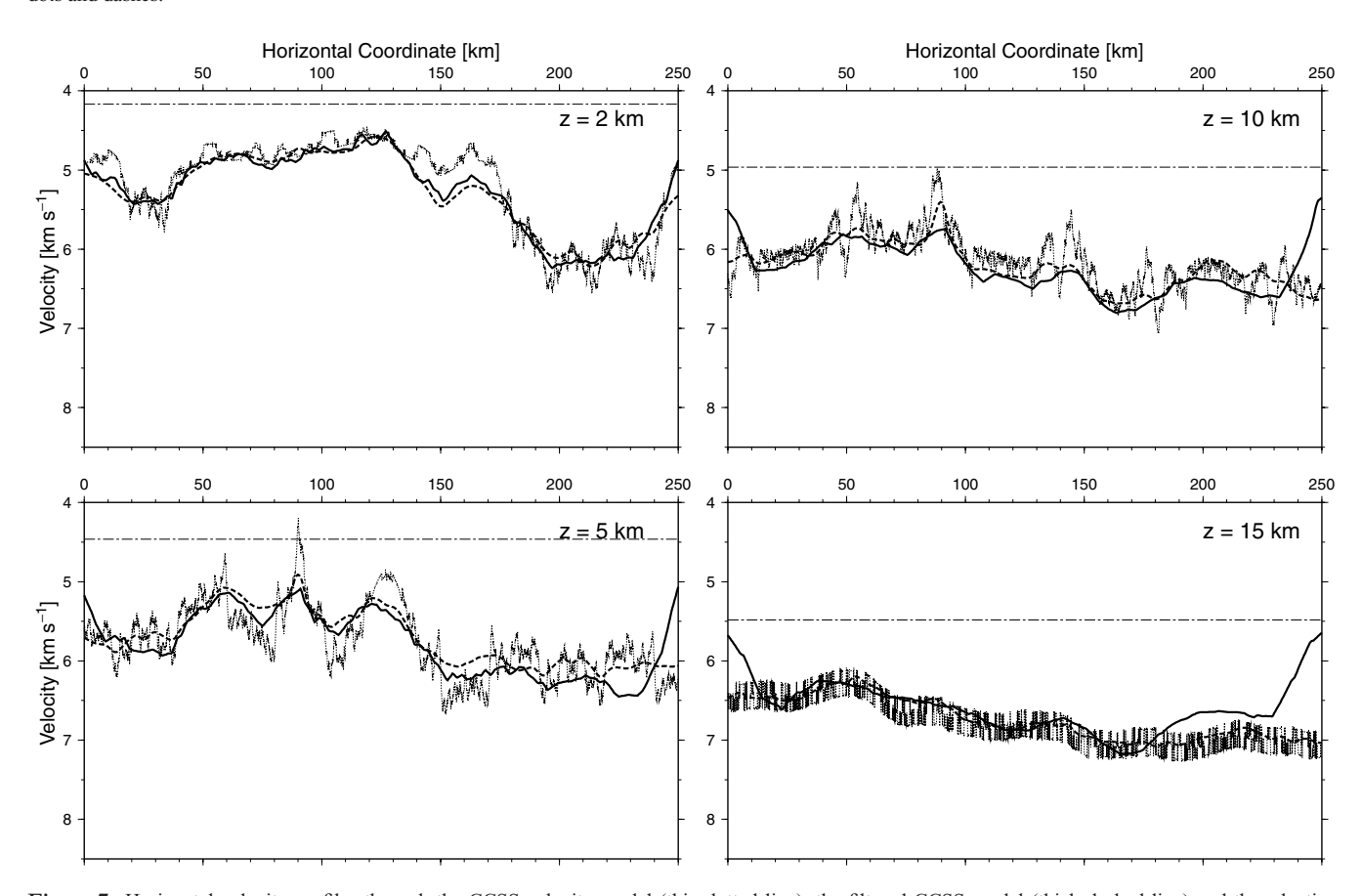


Figure 7. Horizontal velocity profiles through the CCSS velocity model (thin dotted line), the filtered CCSS model (thick dashed line) and the adaptive inversion result (thick solid line) for constant depths of 2, 5, 10 and 15 km. The velocity in the starting model is shown as a thin line with alternating dots and dashes.

et al. (2002a) we decided to use the same traveltime data as input for our joint velocity and interface inversion. The starting model for the inversion consisted of seven layers (Fig. 9a). The seafloor was fixed and taken from the result obtained by Bosch et al. (2002b) (Fig. 9c). Horizontal interfaces were located in the starting model for the new inversion approach at 2.0, 2.5, 3.5, 4.5 and 7.0 km depth. The velocity of the first layer was fixed to 1.49 km s⁻¹, and the other layers had a velocity of 2.1 km s⁻¹ at 2.0 km depth with a vertical velocity gradient of $0.5 \, \mathrm{s}^{-1}$ assigned. All interfaces and velocities

of layers below the seafloor were subjected to a simultaneous inversion. The side length of the regular triangles in all grids was 3.5 km. Horizontal and vertical covariance ranges for the inversion of the velocities in the individual layers are listed in Table 1. The lateral covariance range for the interface nodes was set to 2.0 km for all interfaces.

The eight phases used in the inversion were reflections from the first, second, and third sediment reflectors, reflections from the top of the sills, and long-offset reflections from the top of the basement.

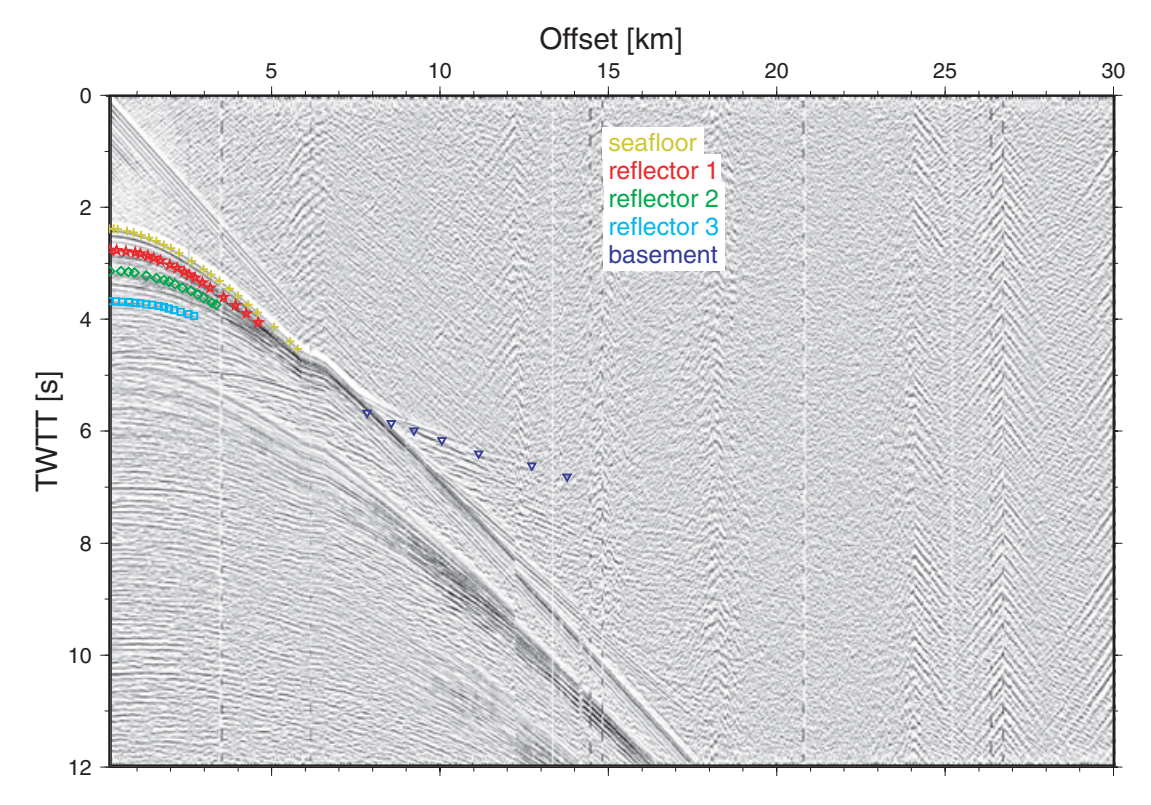


Figure 8. Example shot super-gather with picks superimposed (source at 45 km horizontal coordinate).

Turning rays were included from within the sediments just above the sills, from within the sub-sill sediments, and from within the basement. All eight phases were used simultaneously in the joint interface and velocity inversion.

The inversion result after eight iterations is shown in Fig. 9(b). The region of no ray coverage (final iteration) is shaded pale. The result obtained by Bosch et al. (2002b) is shown for comparison in Fig. 9(c). The difference between Figs 9(b) and (c) and the interfaces of both results are plotted in Fig. 9(d). We see that sediment and sill interfaces match well and that their local trends are in good agreement. The sill interface obtained with the new algorithm seems to be more plausible than the strongly oscillating interface derived by Bosch et al. (2002b), shown in Fig. 9(c). The results differ most for the basement interface. The general structure, consisting of a central high and deeper regions to both sides, is recovered with both methods. The velocities of Figs 9(b) and (c) match well. Note the agreement for the low-velocity zone in the second sedimentary layer between 54 and 65 km horizontal coordinate, the zone of higher velocity just underneath in the next layer, and especially the region of high velocity above the basement between 37.5 and 46 km horizontal coordinate. The velocity of the new result in the basement high between 44 and 50 km horizontal coordinate is not well constrained, since there is little ray coverage in this region, with hardly any crossing ray paths.

The comparison between the model obtained with the new algorithm and the results presented by Bosch *et al.* (2002b) demonstrates that the new method is very well suited to performing a joint velocity and interface inversion. Furthermore, this experiment confirms independently the same general structure of the area obtained from two different inversion methods.

Fig. 10 shows the seismic section after post-stack depth migration using the velocity model obtained with the new traveltime tomography algorithm. The upper part of the model down to the sills is

well resolved within the region of ray coverage (between 37.5 and 66 km horizontal coordinate). The interfaces for the three sedimentary reflectors agree with the seismic image. In the case of the interface that was chosen to represent the discontinuous sill reflectors it can be seen that the general trend fits the major reflective events. The basement interface does not seem to match structures in the seismic section, except for the region between 33 and 37 km horizontal coordinate, where maybe the shadow of a rotated basement block is visible. In order to improve the inversion result in the deeper region of the model additional traveltime picks may be used to constrain the model. However, the low signal-to-noise ratio for reflected and refracted events from below the basalt as well as the difficulty in assigning the correct ray path to a long-offset refracted event render the task difficult in this case.

5 CONCLUSIONS

A new 2-D traveltime tomography method has been presented that is able to efficiently simulate and invert densely sampled seismic long-offset reflection and refraction data. The method makes use of an adaptive model parametrization, optimizing the number of parameters involved in the inversion and allowing great flexibility in model definition. The semi-analytical ray-tracing procedure allows fast and accurate forward modelling through the triangulated grids. Velocity and interface Fréchet derivatives are calculated analytically, allowing a linearized inversion approach to the non-linear problem. Regularization based on model covariances allows the inclusion of a priori knowledge and adaptive smoothing constraints.

An inversion test performed on a synthetic crustal model demonstrated superior results obtained with adaptive model parametrization and inversion regularization compared with non-adaptive parametrization. Starting with a coarse model parametrization, the

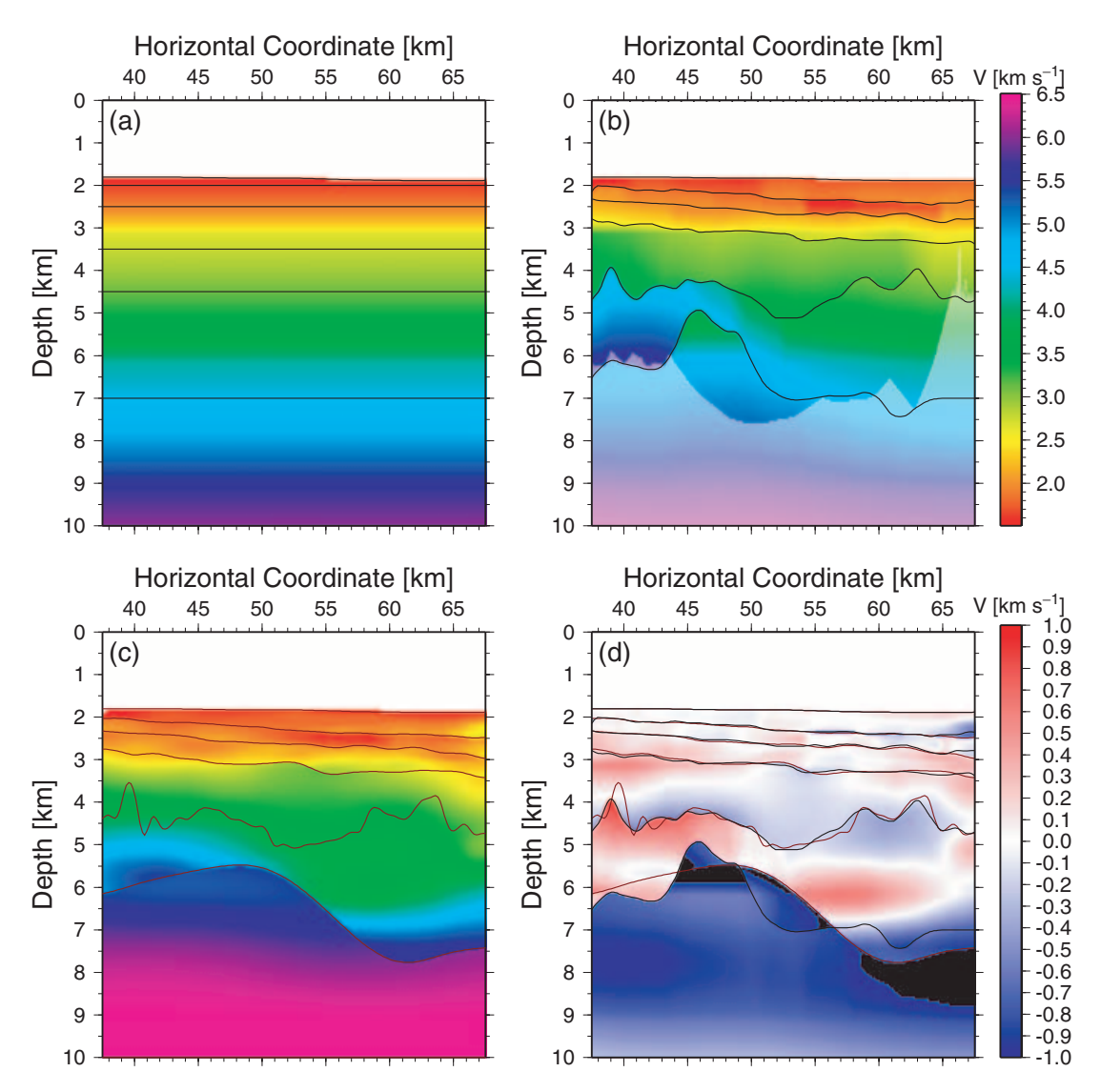


Figure 9. Comparison between results obtained with the new traveltime tomography algorithm and results obtained by Bosch *et al.* (2002b). (a) Starting model for the inversion with the new algorithm. (b) The corresponding inversion result after eight iterations obtained by using the same traveltime data as Bosch. The region of no ray coverage is shaded pale. (c) Result obtained by Bosch *et al.* (2002b). (d) Difference between (b) and (c). The black region in (d) is due to velocities beyond the range of the colour scale. Parts (a), (b) and (c) all use the same colour scale.

Table 1. Horizontal (Δa_x) and vertical (Δa_z) covariance ranges used in the inversion for the individual layers.

Layer	Δa_x covariance [km]	Δa_z covariance [km]
Seawater	_	_
Sediment 1	4.0	0.5
Sediment 2	4.0	0.5
Sediment 3	4.0	0.5
Sediment 4	4.0	1.0
Sediment 5	15.0	1.0
Basement	18.0	2.0

long-wavelength features of the model are recovered. With decreasing misfit the model parametrization is refined, allowing more detail to emerge.

A second inversion test using real seismic long-offset traveltime data resulted in the recovery of an interface—velocity model. The comparison with independently obtained results showed good agreement. While the velocity model is well determined in the upper part,

it is less certain in the deeper region due to the difficulty of obtaining data for weak sub-basalt events, which limits the capabilities of the inversion in this case. This result demonstrates the ability of the new algorithm to invert densely sampled refraction and reflection data successfully.

The new algorithm is a suitable tool for the traveltime inversion of densely sampled seismic data sets, providing velocity models that can be used as starting models for more advanced inversion techniques, such as full-waveform inversion, or to be used for prestack depth migration.

ACKNOWLEDGMENTS

We thank Colin Zelt and John Hole for providing the model and data used in the synthetic inversion test. We wish to acknowledge the Rockall Consortium for providing the seismic data used in this study. We thank Hassan Masoomzadeh and Richard Hobbs for technical and scientific support. The free software GMT (Wessel & Smith 1991) was used for the generation of figures. This work was

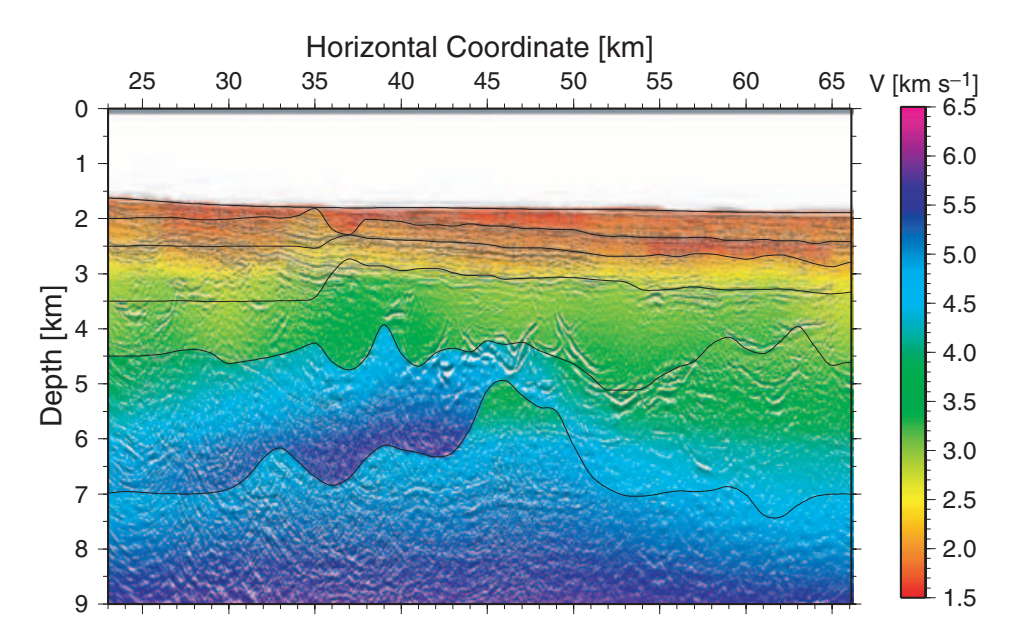


Figure 10. This section was post-stack depth-migrated using the velocity model obtained by tomographic inversion. The stack is illuminated with the velocities of the inversion result and the corresponding interfaces are superimposed (from top: seafloor, reflector 1, reflector 2, reflector 3, sill, basement). The interfaces for the three upper sedimentary reflectors as well as the interface representing the discontinuous sill agree well with the seismic image. The basement interface and the velocity below the sill interface are questionable due to the small number of data and thus the low ray coverage in this region.

funded by the sponsors of the LITHOS project [Agip (UK) Ltd, Amerada Hess Ltd, BP Amoco Exploration Operating Co Ltd, Conoco (UK) Ltd, ExxonMobil International Ltd, Japan Petroleum Exploration Ltd, Lasmo Plc, ONGC India, Norsk Hydro ASA, Ranger Oil (UK) Ltd, Schlumberger Cambridge Research, Shell UK Ltd, Texaco Britain Ltd, TotalFinaElf Exploration UK Plc, Veritas DGC Ltd]. We also thank Aldo Vesnaver and an anonymous reviewer for their constructive comments which significantly improved the original manuscript.

REFERENCES

Bishop, T.N., Bube, K.P., Cutler, R.T., Langan, R.T., Love, P.L., Resnick, J.R., Shuey, R.T., Spindler, D.A. & Wyld, H.W., 1985. Tomographic determination of velocity and depth in laterally varying media, *Geophysics*, 50, 903–923.

Böhm, G. & Vesnaver, A., 1996. Relying on a grid, *J. seism. Explor.*, 5, 169–184.

Böhm, G., Galuppo, P. & Vesnaver, A., 2000. 3D adaptive tomography using Delaunay triangles and Voronoi polygons, *Geophys. Prospect.*, 48, 723–744

Bosch, M., Barton, P. & Singh, S., 2002a. Geostatistical tomography of short and long offset seismic data from the NE Atlantic Margin, 64TH Mtg. EAGE, Expanded Abstracts, P174.

Bosch, M., Barton, P. & Singh, S.C., 2002b. Travel-time tomography combining short and long offset arrivals, Tech. Report:, *LITHOS*, ISSN 1476–2706, Cambridge University, 43–46.

Červený, V., 2001. Seismic Ray Theory, Cambridge Univ. Press, Cambridge. Cox, B. & Verschuur, D.J., 2001. Tomographic inversion of focusing operators, EAGE, Expanded Abstracts, 63rd Mtg, M35.

Dubrule, O., 2003. Geostatistics for seismic data integration in earth models: 2003 Distinguished Instructor Short Course & EAGE, SEG.

England, R.W. & Hobbs, R.W., 1997. The structure of the Rockall Trough imaged by deep seismic reflection profiling, J. geol. Soc. Lond., 154, 497– 502

Failly, M., Singh, S.C. & Hobbs, R.W., 1993. Lower crustal reflectivity from waveform inversion, *Geophys. J. Int.*, 115, 410–420. Faletič, R., 1997. Seismic tomography with a self-adaptive parameterization, *PhD thesis*, Australian National University, Canberra.

Farra, V., 1990. Amplitude computation in heterogenous media by ray perturbation theory: a finite element approach, *Geophys. J. Int.*, 103, 341–354.
 Fortune, S.J., 1987. A sweepline algorithm for Voronoi diagrams, *Algorithmica*, 2, 153–174.

Freudenreich, Y., 2002. Full waveform inversion, PhD thesis, University of Cambridge, Cambridge.

Hale, D. & Cohen, J. K., 1991. Triangulated models of the Earth's subsurface, Tech. Report, Center for Wave Phenomenon Report, CWP-107. Colorado School of Mines. Golden.

Hobro, J., 1999. Three-dimensional tomographic inversion of combined reflection and refraction seismic traveltime data, *PhD thesis*, University of Cambridge, Cambridge.

Hobro, J.W.D., Singh, S.C. & Minshull, T.A., 2003. Three-dimensional tomographic inversion of combined reflection and refraction seismic traveltime data, *Geophys. J. Int.*, 152, 79–93.

Hoff, K., 1996. Explorations in Geometric Modeling: Parametric Curves and Surfaces COMP236 Final Project Report, University of North Carolina at Chapel Hill.

Hua, B. & Liu, F., 1995. Joint reflection imaging of velocity and interface— Theory and method, ACTA Geophys. Sinica, 38(6), 750–756.

Hubral, P. & Krey, T., 1980. Interval velocities from seismic reflection traveltime measurements, *SEG*, Tulsa.

Indira, N.K. & Gupta, P.K., 1998. Inverse Methods—General Principles and Applications to Earth System Sciences, Narosa Publishing House, London.

Isaaks, E.H. & Srivastava, R.M., 1989. An Introduction to Applied Geostatistics, Oxford University Press, Oxford.

Joppen, M. & White, R.S., 1990. The structure and subsidence of Rockall Trough from two-ship seismic experiment, *J. geophys. Res.*, 95, 19821– 19837.

Kissling, E., Husen, S. & Haslinger, F., 2001. Model parameterization in seismic tomography: a choice of consequence for the solution quality, *Phys. Earth planet. Inter.*, 123, 89–101.

Korenaga, J., Holbrook, W.S., Singh, S.C. & Minshull, T.A., 1997. Natural gas hydrates on the southeast U.S. margin: Constraints from full waveform and travel time inversions of wide-angle seismic data, *J. geophys. Res.*, 102, 15 345–15 365.

- Kormendi, F. & Dietrich, M., 1991. Nonlinear waveform inversion of planewave seismograms in stratified elastic media, Geophysics, 56, 664–674.
- Lutter, W.L., Catching, R.D. & Jarchow, C.M., 1994. An image of the Columbia Plateau from inversion of high-resolution seismic data, *Geo-physics*, 59, 1278–1289.
- McCaughey, M., 1995. Travel-time tomography of wide-angle seismic data, *PhD thesis*, University of Cambridge, Cambridge.
- McCaughey, M. & Singh, S.C., 1997. Simultaneous velocity and interface tomography of normal-incidence and wide-aperture seismic traveltime data, Geophys. J. Int., 131, 87–99.
- Mosegaard, K. & Tarantola, A., 1995. Monte Carlo sampling of solutions to inverse problems, *J. geophys. Res.*, **100**, 12 431–12 477.
- Muir, F. & Dellinger, J., 1985. A practical anisotrophic system., Stanford Exploration Project Reports, 44, 55–58.
- Phillips, W.S. & Fehler, M.C., 1991. Traveltime tomography: A comparison of popular methods, *Geophysics*, 56, 1639–1649.
- Pratt, R.G., Song, Z.-M., Williamson, P. & Warner, M., 1996. Twodimensional velocity models from wide-angle seismic data by wavefield inversion, *Geophys. J. Int.*, 124, 323–340.
- Pratt, G.R., Fuchun, G., Zelt, C. & Levander, A., 2002. The limits and complementary nature of traveltime and waveform inversion, *J. Conf. Abstracts*, 7, 181–182.
- Press, W.H., Teukolsky, S.A., Vetterling, W.T. & Flannery, B.P., 1992. Numerical Recipes in C The Art of Scientific Computing, Cambridge University Press, Cambridge.
- Roberts, D.G., Thompson, M., Mitchener, B., Hossack, J., Carmichael S. & Bjornseth, H.-M., 1999. Palaeozoic to Tertiary rift and basin dynamics: mid-Norway to the Bay of Biscay—a new context for hydrocarbon prospectivity in the deep water frontier, in, *Petroleum Geology of Northwest Europe, Proc. 5th Conf.*, Vol 1, pp. 7–40, Fleet, A.J. & Boldy, S.A.R. The Geological Society, London.
- Sambridge, M., Braun, J. & McQueen, H., 1995. Geophysical parameterization and interpolation of irregular data using natural neighbours, *Geophys. J. Int.*, **122**, 837–857.
- Scales, J.A., 1987. Tomographic inversion via the conjugate gradient method, *Geophysics*, **52**, 179–185.
- Scales, J.A. & Smith, M.L., 1997. Introductory Geophysical Inverse Theory, Samizdat Press, Colorado School of Mines, Golden. http://samizdat.mines.edu.
- Sheriff, R.E. & Geldart, L.P., 1995. Exploration Seismology, Cambridge University Press, Cambridge.
- Shipp, R.M. & Singh, S.C., 2002. Two-dimensional full wavefield inversion of wide-aperture marine seismic streamer data, *Geophys. J. Int.*, 151, 325– 344.
- Shirley, P., 1992. Polygon Intersection via Barycentric Coordinates, *Ray Tracing News*, **5**(3).http://www.acm.org/tog/resources/RTNews/html/rtnv5n3.html
- Soupios, P.M., Papazachos, B.C. & Tsokas, G.N., 1999. Simultaneous determination of velocity and interface depth in reflection tomography, Second Balkan Geophysical Congress and Exhibition, O3-3. pp. 10–11, Balkan Geophysical Society, Bucharest, Romania.
- Tarantola, A., 1987. Travel time and seismic waveform inversion, in, Seismic Tomography, pp. 135–157, ed. Nolet, G., Reidel, Dordrecht.
- Tarantola, A. & Valette, B., 1982. Inverse Problems = Quest for Information, J. Geophys., 50, 159–170.
- Vesnaver, A., 1994. Towards the uniqueness of tomographic inversion solutions, J. seism. Explor., 3, 323–334.
- Wessel, P. & Smith, W.H.F., 1991. Free software helps map and display data, *EOS, Trans. Am. geophys. Un.*, **72**, 441.
- Yilmaz, O., 1987. Seismic Data Processing, ed. Doherty, S.M., SEG, Tulsa.Zeev, N., Savasta, O. & Cores, D., 2001. Full Waveform Inversion Using the Nonmonotone Spectral Projected Gradient Method, 63rd Mtg.: EAGE, Session: P011.
- Zelt, C.A. & Barton, P.J., 1998. Three-dimensional seismic refraction tomography: A comparison of two methods applied to data from the Faroe Basin, J. geophys. Res., 108, 7187–7210.
- Zelt, C.A. & Smith, R.B., 1992. Seismic traveltime inversion for 2-D crustal velocity structure, *Geophys. J. Int.*, **108**, 16–34.

APPENDIX A: LINEAR INTERPOLATION IN A TRIANGLE

The formula for the linear interpolation of a value q defined at the vertices of a triangle at location \mathbf{x} within the triangle is

$$q(\mathbf{x}) = q_0 + \nabla q \cdot (\mathbf{x} - \mathbf{x}_0), \tag{A1}$$

with q_0 being the value of q at location \mathbf{x}_0 , and ∇q as the gradient of the scalar field of q. Knowing the values q_i at the vertices \mathbf{x}_i and expressing the differences with respect to the first vertex, the gradient can simply be found from

$$\nabla q = \begin{pmatrix} (\mathbf{x}_2 - \mathbf{x}_1)^{\mathrm{T}} \\ (\mathbf{x}_3 - \mathbf{x}_1)^{\mathrm{T}} \end{pmatrix}^{-1} \begin{pmatrix} q_2 - q_1 \\ q_3 - q_1 \end{pmatrix} = \mathbf{X} \begin{pmatrix} q_2 - q_1 \\ q_3 - q_1 \end{pmatrix}, \tag{A2}$$

where **X** is a 2×2 matrix.

APPENDIX B: DEFINITION OF INTERFACES

The cubic Hermite polynomial f(x) is used to interpolate the interface between node points based on the coordinate information of the nodes (x_1, z_1) and (x_2, z_2) and the interface depth gradients $f'(x_1)$ and $f'(x_2)$. The cubic Hermite polynomial f(x) is defined as (Hoff 1996)

$$f(x) = Ax^3 + Bx^2 + Cx + D,$$
 (B1)

with

$$A = 2(f(x_1) - f(x_2)) + f'(x_1) + f'(x_2),$$
(B2)

$$B = 3(f(x_2) - f(x_1)) - 2f'(x_1) - f'(x_2),$$
(B3)

$$C = f'(x_1), (B4)$$

$$D = f(x_1), (B5)$$

and the constraint that $f(x_1) = 0$ and $f(x_2) = 1$. In matrix notation we can write

$$\mathbf{U} = \begin{pmatrix} x^3 \\ x^2 \\ x \\ 1 \end{pmatrix},\tag{B6}$$

$$\mathbf{H} = \begin{pmatrix} 2 & -2 & 1 & 1 \\ -3 & 3 & -2 & -1 \\ 0 & 0 & 1 & 0 \\ 1 & 0 & 0 & 0 \end{pmatrix},\tag{B7}$$

$$\mathbf{G} = \begin{pmatrix} f(x_1) \\ f(x_2) \\ f'(x_1) \\ f'(x_2) \end{pmatrix}, \tag{B8}$$

and the interface depth for any value x between x_1 and x_2 becomes

$$f(x) = \mathbf{U}^{\mathrm{T}} \cdot \mathbf{H} \cdot \mathbf{G}. \tag{B9}$$

APPENDIX C: FRÉCHET DERIVATIVE CALCULATION

C1 Velocity parameter Fréchet derivatives

The effect of small changes in the velocity of a model parameter will be related to changes in traveltime. The traveltime T in an isotropic medium is the integral over the slowness u along the ray:

$$T = \int_{s_1}^{s_2} u \ ds, \tag{C1}$$

with the arclength s. The partial derivative of the traveltime with respect to model parameter m, which represents the u^2 values at the three velocity node points of each triangle, can be written as

$$\frac{\partial T}{\partial m} = \frac{\partial}{\partial m} \int_{s_1}^{s_2} u \ ds. \tag{C2}$$

Assuming no change to the ray path according to Fermat's principle one can write

$$\frac{\partial T}{\partial m} = \int_{s_1}^{s_2} \frac{\partial u}{\partial m} \, ds. \tag{C3}$$

With the ray sampling variable τ instead of the arclength s, where $ds = u \ d\tau$, we can write

$$\frac{\partial T}{\partial m} = \int_{\tau_1}^{\tau_2} \frac{\partial u}{\partial m} u \ d\tau. \tag{C4}$$

Since $\partial(u^2) = 2u \ \partial u$, it follows that

$$\frac{\partial T}{\partial m} = \frac{1}{2} \int_{\tau_1}^{\tau_2} \frac{\partial (u^2)}{\partial m} d\tau. \tag{C5}$$

Differentiating eq. (1) with respect to model parameter m gives

$$\frac{\partial \left(u^2(\mathbf{x})\right)}{\partial m} = \frac{\partial \left(u_0^2\right)}{\partial m} + \frac{\partial \Gamma}{\partial m} \cdot \mathbf{x}(\tau),\tag{C6}$$

and substituting eq. (4) into eq. (C6) we obtain

$$\frac{\partial u^2(\mathbf{x})}{\partial m} = \frac{\partial u_0^2}{\partial m} + \frac{\partial \mathbf{\Gamma}}{\partial m} \cdot \left[\frac{1}{4} \mathbf{\Gamma} (\tau - \tau_0)^2 + \mathbf{p}(\tau_0) (\tau - \tau_0) + \mathbf{x}(\tau_0) \right],\tag{C7}$$

Eq. (C7) can be written as a quadratic function of τ :

$$\frac{\partial u^{2}(\mathbf{x})}{\partial m} = \frac{1}{4} \frac{\partial \mathbf{\Gamma}}{\partial m} \cdot \mathbf{\Gamma} (\tau - \tau_{0})^{2} + \frac{\partial \mathbf{\Gamma}}{\partial m} \cdot \mathbf{p}(\tau_{0})(\tau - \tau_{0}) + \frac{\partial \mathbf{\Gamma}}{\partial m} \cdot \mathbf{x}(\tau_{0}) + \frac{\partial (u_{0}^{2})}{\partial m}.$$
(C8)

Substituting eq. (C8) into eq. (C5) and subsequent integration yields

$$\frac{\partial T}{\partial m} = \frac{1}{2} \left[\frac{1}{12} \frac{\partial \mathbf{\Gamma}}{\partial m} \cdot \mathbf{\Gamma} (\tau - \tau_0)^3 + \frac{1}{2} \frac{\partial \mathbf{\Gamma}}{\partial m} \cdot \mathbf{p} (\tau_0) (\tau - \tau_0)^2 + \left(\frac{\partial \mathbf{\Gamma}}{\partial m} \cdot \mathbf{x} (\tau_0) + \frac{\partial (u_0^2)}{\partial m} \right) (\tau - \tau_0) \right].$$
(C9)

If $q = u^2$ in eqs (A1) and (A2) then nabla; $q = \mathbf{\Gamma}$. Differentiating expression (A2), we have

$$\frac{\partial \mathbf{\Gamma}}{\partial u_1^2} = -\mathbf{X} \begin{pmatrix} 1\\1 \end{pmatrix},\tag{C10}$$

$$\frac{\partial \mathbf{\Gamma}}{\partial u_2^2} = \mathbf{X} \begin{pmatrix} 1\\0 \end{pmatrix},\tag{C11}$$

$$\frac{\partial \mathbf{\Gamma}}{\partial u_3^2} = \mathbf{X} \begin{pmatrix} 0 \\ 1 \end{pmatrix}. \tag{C12}$$

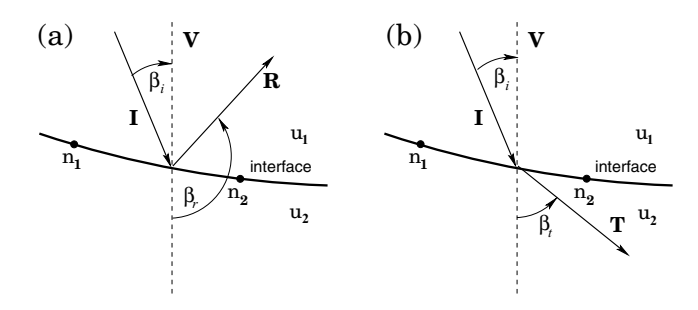


Figure C1. (a) Reflection and (b) transmission at an interface with the slowness vectors of the incident, reflected, and transmitted rays \mathbf{I} , \mathbf{R} , and \mathbf{T} . β_1 is the angle between \mathbf{I} and the vertical \mathbf{V} , while β_r and β_t are the angles between \mathbf{R} , respectively \mathbf{T} , and \mathbf{V} . u_1 and u_2 are the slowness values of the first and second medium. n_1 and n_2 are the relevant interface nodes.

Differentiating eq. (A1),

$$\frac{\partial u_0^2}{\partial u_1^2} = 1 - \frac{\partial \mathbf{\Gamma}}{\partial u_1^2} \cdot (\mathbf{x_1} - \mathbf{x_0}),\tag{C13}$$

$$\frac{\partial u_0^2}{\partial u_2^2} = -\frac{\partial \mathbf{\Gamma}}{\partial u_2^2} \cdot (\mathbf{x_1} - \mathbf{x_0}),\tag{C14}$$

$$\frac{\partial u_0^2}{\partial u_2^2} = -\frac{\partial \mathbf{\Gamma}}{\partial u_2^2}.(\mathbf{x}_1 - \mathbf{x}_0). \tag{C15}$$

In order to be able to update the velocity of the model it is necessary to convert the Fréchet derivatives with respect to u^2 to Fréchet derivatives with respect to velocity v. This is achieved by multiplication of $\partial T/\partial u^2$ with $\partial(u^2)/\partial v = -2/v^3$, so that

$$\frac{\partial T}{\partial v} = -\frac{2}{v^3} \frac{\partial T}{\partial u^2}.$$
 (C16)

C2 Interface parameter Fréchet derivatives

Interface Fréchet derivatives are computed for all interface nodes whose depths have an effect on the traveltime of rays. The procedure steps along every ray in the model and determines the ray—interface intersections, discriminating between the transmission and reflection cases. Formulations for the calculation of traveltime derivatives for interface depth can be found in Bishop *et al.* (1985), McCaughey (1995), or Hua & Liu (1995). We follow the description of McCaughey (1995) since it is based on the slowness vectors of incident, reflected, and transmitted rays, and was therefore easy to implement. In the scheme presented here, traveltime derivatives for the horizontal coordinate of the interface node are not taken into account. This means that interface nodes may move only vertically during the inversion.

The angle β_i between the slowness vectors of the incident ray **I** and the vertical **V** (Fig. C1) is identical for the transmission and the reflection case. It can be calculated via the following expression:

$$\cos \beta_{i} = \frac{\mathbf{I} \cdot \mathbf{V}}{|\mathbf{I}| \cdot |\mathbf{V}|}.\tag{C17}$$

In the case of the reflected ray (Fig. C1a), the angle $\beta_{\rm r}$ between the slowness vector of the reflected ray ${\bf R}$ and the vertical ${\bf V}$ replaces $\beta_{\rm i}$ in eq. (C17) and ${\bf R}$ replaces ${\bf I}$, while in the case of transmission (Fig. C1b), $\beta_{\rm i}$ is replaced by the angle $\beta_{\rm t}$ between the slowness vector of the transmitted ray ${\bf T}$ and the vertical ${\bf V}$, and ${\bf I}$ is replaced by ${\bf T}$.

For each ray intersecting an interface we will obtain two Fréchet derivatives, one for each of the two interface nodes n_1 and n_2 on either side of the ray intersection point. In the reflection case the traveltime derivative is

$$\frac{\partial t}{\partial n_i} = u_1(\cos \beta_i - \cos \beta_r) \frac{\partial f}{\partial z_i}, \quad j = 1, 2,$$
 (C18)

where u_1 is the slowness of the primary medium. $\partial z/\partial z_1$ and $\partial z/\partial z_2$ are the partial derivatives of the cubic Hermite polynomial f(x) that describes the interface (eq. B1) with respect to the depths z_1 and z_2 of the nodes n_1 and n_2 :

$$\frac{\partial f}{\partial z_1} = 2x^3 - 3x^2 + 1,\tag{C19}$$

$$\frac{\partial f}{\partial z_2} = -2x^3 + 3x^2. \tag{C20}$$

In the transmission case the Fréchet derivatives for the interface nodes are expressed as

$$\frac{\partial t}{\partial n_j} = (u_1 \cos \beta_i - u_2 \cos \beta_t) \frac{\partial f}{\partial z_j}, \quad j = 1, 2,$$
 (C21)

with u_2 being the slowness of the second medium.